Author's Post-print version. Article published in Combustion and Flame, Volume 213, March 2020, Pages 117-131.
DOI: 10.1016/j.combustflame.2019.11.018
Published version: https://www.sciencedirect.com/science/article/pii/S0010218019305231

A fast-solving particle model for thermochemical conversion of biomass

Tian Li[a,*], Henrik Thunman[b], Henrik Strӧm[c]

[a] *Department of Energy and Process Engineering, Faculty of Engineering, NTNU — Norwegian University of Science and Technology, Trondheim, Norway*
[b] *Division of Energy Technology, Department of Space, Earth and Environment, Chalmers University of Technology, Göteborg, Sweden*
[c] *Division of Fluid Dynamics, Department of Mechanics and Maritime Sciences, Chalmers University of Technology, Göteborg, Sweden*

Abstract

Computational fluid dynamics (CFD) simulations of large-scale furnaces or reactors for thermal conversion of solid fuels remains challenging partially due to the high computational cost related to the particle sub-models. Owing to the thermally thick nature, it is particularly expensive to simulate the conversion of large fuel particles such as biomass particles. To address this issue, a fast-solving particle model was developed in this work with special attention to the computational efficiency. The model spatially discretizes a fuel particle in one homogenized dimension. The conversion process of the fuel particle is treated as a reactive variable-volume one-dimensional transient heat conduction problem. The model also utilizes several features that are typically found in sharp interphase-based models to reduce the computational cost. Validation of the model was carried out by comparing with experimental results under both pyrolysis and combustion conditions. The

*Corresponding author
Email address: tian.li@ntnu.no (Tian Li)

accuracy and computational efficiency of the model was thoroughly examined by varying the degrees of temporal and spatial discretization. It was found that the model well predicted pyrolysis and combustion of a single biomass particle within a broad range of temporal and spatial discretization. The time used to simulate the conversion of a biomass particle using the developed model can be more than one order of magnitude smaller than the conversion process itself. It was also revealed that a well-predicted conductive heat transfer inside the particle is essential for a precise simulation of the drying and devolatilization process. The char conversion process, however, is less sensitive to the external heat transfer as it is mainly controlled by the mass diffusion process. Further studies showed that a time step of 1×10^{-3} s and a spatial discretization of 20 cells were sufficient for simulating the conversion of typical fuel particles in grate-fired and fluidized-bed furnaces. We also demonstrated that when the particle model was implemented in a CFD solver, only 2.2% of computational overhead was introduced by the model. As the model can efficiently employ fixed time stepping, optimal load balancing during parallel computing of many simultaneous conversion processes becomes trivial. This performance opens up new possibilities for treating fuel polydispersity in Eulerian CFD simulations of biomass conversion.
Keywords: biomass, combustion, mathematical modeling, CFD

Nomenclature

Symbols

A pre-exponential factor (1/s)

AC ash content (-)

a matrix coefficient (J/K s)

b matrix coefficient (J/s)

C molar concentration (mol/m^3)

c_p heat capacity (J/kg K)

d initial diameter (m)

dt time step (s)

ΔH heat of reaction (J/kg)

E activation energy (kJ/mol)

h convective heat transfer coefficient (J/m^2 K s)

k_{eff} effective rate constant (m/s)

l initial length of a finite cylinder (m)

l_1,l_2,l_3 initial dimensions of a parallelepiped (m)

M molar mass (kg/mol)

m mass of a given species in a cell (kg)

m_p particle mass (kg)

MC moisture content (-)

Np number of cells (-)

r homogenized radial position (m)

rb particle radius (m)

RCT relative calculation time (-)

RE relative error (%)

S mass source during a given conversion stage (kg/s)

S_g specific gravity (-)

S_p implicit coefficient for the source term of energy equation (J/K s)

S_u explicit contribution to the source term of energy equation (J/s)

S_{energy} source term of energy equation (J/s)

SA surface area (m^2)

SF shrinkage factor during a given conversion stage (-)

t time (s)

T_g gas temperature (K)

T_s solid temperature (K)

T_w reactor wall temperature (K)

t_{HT} timescale of conductive heat transfer (s)

$t_{total,cal}$ total time used for executing the code (s)

$t_{total,con}$ total conversion time of a particle (s)

V volume of a given species in a cell (m^3)

V_c volume of a cell (m^3)

V_p particle volume (m^3)

w mass fraction (-)

xb location of the outer cell boundary (m)

xc location of the cell mass center (m)

Greek

α fraction of oxygen consumed by volatile gases (-)

β mass transfer coefficient (m/s)

Γ particle shape factor (m^2)

ϵ emissivity (-)

θ radiation temperature (K)

κ thermal conductivity (J/m K s)

ρ density (kg/m^3)

σ Stefan Boltzmann constant (kg/s^3 K^4)

ϕ volume fraction (-)

χ coefficient of the explicit discretization of the energy equation (J/K s)

Ω stoichiometric coefficient (-)

Subscript

∞ far field

ash ash

b cell outer boundary i.e. west boundary

BL baseline

C carbon atom

$char$ char

$charc$ char conversion process

$charf$ char front

db dry based

dev devolatilization process

dry drying process

dry_wood dry wood

E east cell

gas gas

H hydrogen atom

$H2O$ water molecule

O oxygen atom

$O2$ oxygen molecule

P cell center

sur particle surface

tar tar

vol volatiles

W west cell

wb wet based

wet_wood wet wood

Superscript

$*$ current time step

0 previous time step

Abbreviations

CFD computational fluid dynamics

DEM discrete element method

IBM interface-based model

MBM mesh-based model

ODE ordinary differential equation

PDE partial differential equation

SFOR single first-order

SIMPLE semi-implicit method for pressure linked equations

1. Introduction

Biomass is a promising renewable source of heat, power, liquid fuels, and chemicals. It has gained popularity due to the increased awareness of sustainability, especially for the lignocellulosic biomass, which has been widely used in the Nordic countries to replace fossil fuels [1]. Due to the fibrous nature of lignocellulosic biomass, it is energy-intensive to reduce the size of a biomass particle. Consequently, biomass fuel particles used in industrial-sized furnaces are usually much bigger than coal particles. Moreover, the proportion and rate of release of volatiles differ significantly between coal and biomass. This situation makes the often-used thermally thin assumption (i.e. negligible internal temperature gradients) in the modelling of coal conversion less suitable when simulating conversion of biomass. In addition, a recent study has suggested that temperature gradients inside a biomass particle need to be considered even under suspension-firing conditions [2], where the majority of fuel particles are less than 500 μm. The internal temperature field not only influences the rate of conversion, but also to a great extent the biomass decomposition products.

To more accurately simulate the conversion of biomass particles, non-isothermal models accounting for the thermal thickness have been developed, ranging from simplified one-dimensional modelling approaches to comprehensive multi-dimensional models. A comprehensive overview of these various modelling approaches has been presented recently [3], in which multi-

dimensional models are recommended only when there is a need to account for the anisotropy of the fuel particle or when the boundary conditions of the fuel particle are varying significantly in space [3]. Both these scenarios are, however, rare in large-scale biomass-fueled reactors. Despite the anisotropy of the raw lignocellulosic biomass, the fuel particles used in industrial-size furnaces can generally be characterized as isotropic due to pretreatments such as size reduction and densification. Even where this is not the case, such as for wood chip fuels, the accuracy obtained from one-dimensional particle models is usually satisfactory without accounting for particle anisotropy [3]. The assumption of homogeneous boundary conditions for the fuel particle is also typically acceptable [4] since the size of a fuel particle is much smaller than that of the fuel bed. Moreover, one-dimensional particle models are also typically linked to the surface area per unit volume of the particle phase, rather than to the surface area of an individual particle, when used in Eulerian fixed-bed reactor models [5]. Consequently, one-dimensional models with their associated reduction in computational cost are in general well suited to simulations of fuel particle conversion in large-scale biomass-fueled reactors. This fact is even more pronounced when the particle conversion model is to be coupled to a computational fluid dynamics (CFD) solver, as but one out of many sub-models in what necessarily becomes a rather computationally expensive configuration.

Generally, one-dimensional models can be categorized into two conceptual groups: interface-based models (IBMs) [5, 6, 7, 8, 9] and mesh-based models (MBMs) [10, 11, 12, 13, 14, 15, 16, 17]. In the IBM, the fuel particle is divided into three (moist wood, dry wood, and char) or four (moist wood,

dry wood, char, and ash) distinct layers. The chemical reactions and phase changes are then described as occurring only in narrow regions between the different layers (i.e. at sharp interfaces). With such a spatial discretization, the governing equations for each layer become ordinary differential equations (ODEs) coupled via boundary conditions at the interfaces. Thus, very few equations and variables need to be solved and stored respectively, and the relatively low memory requirements were also a main driving force for the original development of these types of methods. In the MBM, a particle is discretized along the radius into an ensemble of mesh points over which the conservation equations are spatially discretized. Unlike the IBMs, each discretized unit/cell may contain several different species in the MBM. All governing partial differential equations (PDEs) are converted into an algebraic equation system by discretization in space and time. Depending on the gradients of temperature and species mass fractions, various numbers of grid points are needed for a reasonable representation of the particle conversion process. In some combustion cases, the grid points for a single fuel particle can be as many as 1200 [10], which potentially provides information in much greater spatial detail compared to the more coarsely discretized interface-models.

The IBMs are intuitively believed to have a higher numerical efficiency than the MBMs due to the reduced number of equations. Comparative studies between IBMs and MBMs are however rarely reported. It was briefly stated in a previous study [7] that the developed IBM could achieve a similar level of accuracy as a more comprehensive MBM [15] but at lower computational cost. However, it is worth noting that IBMs have some inherent

characteristics, which may limit their computational performance. For instance, two different sets of energy equations need to be solved sequentially at the boundaries and layers, since the solutions of the algebraic equations at the boundaries provide boundary temperature data that need to be known to advance the layer temperatures in time. Typically, a higher-order explicit method [7] or an iterative implicit method [6] is used to solve the ordinary differential equation for the layer temperatures. However, the accuracy of both methods, as well as the robustness of the explicit method, is in practice limited by the smallest thermal mass of any present layer, indicating that very small time steps are needed in the beginning and towards the end of each conversion process (drying, devolatilization and combustion). Some sort of adaptive time stepping is therefore typically required, as well as a numerical limiter on the smallest layer or particle size allowed [5, 18]. On the other hand, it is common that linearly implicit extrapolation methods are utilized in the MBMs, which can be very efficient particularly when the size of the matrix is small. One reason for the high computational cost of the traditional MBMs is the consideration of intraparticle flow, which is usually ignored in the IBMs. In traditional MBMs, five sets of transport equations need to be solved of which four are related to the gas phase (continuity, momentum, energy, and species). The convective timescale of the off-gas may be smaller, if not comparable, to the timescale of conductive heat transfer in the solid phase, thus, resulting a lower maximum allowed time step. A simplified MBM without solving intraparticle flow may therefore achieve a good balance between accuracy and computational efficiency.

Even though the different types of particle models discussed here form the

basis for comprehensive CFD simulations of reactors for biomass conversion, the implications of the particle model formulation for the computational efficiency of the overall simulation framework are in general not discussed in depth. In particular, biomass combustion systems are typically characterized by a strong flow-chemistry coupling and chemical time-scales that are several orders of magnitude smaller than those relevant for the global conversion process [19]. In such situations, it is customary to invoke operator-splitting and compute the source terms in the energy and species transport equations for the duration of a fluid-flow time step [20, 21]. This repeated stopping and re-initialization of the biomass conversion sub-model has profound consequences for the global efficiency of the numerical method. For example, higher-order time integration methods require storing of information from multiple previous time levels and are associated with a larger computational effort concentrated to the beginning of each CFD time interval [21]. Such methods, which may exhibit superior performance to lower-order alternatives in stand-alone codes, can therefore, perhaps somewhat unexpectedly, deteriorate the overall performance of the final CFD implementation. In the present work, we therefore choose to focus on the balance between computational efficiency, numerical accuracy and predictive capability achievable for biomass particle conversion models intended for use in biomass conversion reactor assessment.

Our long-term ambition with the current work goes further than a mere reduction in the computational cost of particle sub-models in biomass conversion simulations. We target our particle model development at a CFD simulation scenario where the fluid flow time step is in the order of 1×10^{-3}

s or less. If a particle model can be derived such that the computational overhead in a typical fixed-bed conversion simulation is lower than e.g. 10%, then new opportunities will present themselves. More specifically, if the cost of executing one instance of the particle model is small enough, more instances can be afforded with little penalty to the overall computational cost. These additional instances could enable a more elaborate treatment of particle polydispersity or finer spatial resolution in Eulerian simulations. The success of such a computational setup would also in practice depend on the possibilities to achieve efficient parallelization of many simultaneous particle conversion processes. We shall return to these possibilities in the discussion of the results.

The remainder of this paper is organized as follows. In Section 2, a simplified MBM is presented. Besides neglecting the demanding solution of the intraparticle gas flow, the proposed model combines the concept of sharp reaction fronts from the IBM and the advantage of the traditional MBM by using an efficient matrix solver (LU factorization). The modeling details of phase change, reaction, thermophysical parameters, and solution strategy are also described. Validation of the model is discussed in Section 3 by comparing with the experimental data and results from an IBM. In Section 4, comprehensive analysis of the model is carried out to systematically scrutinize effects of model formulation on the predictability and computational efficiency in various conditions. A specific aim is to establish a solid theoretical foundation for interpretations of the observed results. Moreover, general guidelines for CFD simulations using one-dimensional thermally thick particle sub-models are given, and new possibilities offered by the herein presented

particle model are discussed.

2. Theory

2.1. Model framework

As the present model is developed based on an, in our opinion, well-established baseline model [5, 6], implementation details regarding the physicochemical modeling of the conversion processes are not discussed in detail here. We have strived to achieve as similar implementations as the overarching model frameworks allow. The same argument can be made for the choice of material and transport properties – it is not the main purpose here to assess the relative merits of different correlations and literature sources on these values, but to illustrate, analyze and contrast the model behaviors for an acceptable set of property values typical of thermochemical conversion of woody biomass. The main differences between the present MBM, comprehensive MBMs, and IBMs are summarized in Table 1 (the characteristic features of comprehensive MBMs and IBMs are exemplified using previous works [6, 15]). It should be noted that, although there is no direct resolution of gas-phase species concentration fields in the present MBM or in classical IBMs, effects of chemical reactions on outflowing gases may still be included in these modelling frameworks by integration of the reaction rate expressions, given that the residence time through the exterior layers and an approximate temperature profile in these layers are always known.

2.2. Particle heat balance

In the discretized particle model proposed in the current work, the thermochemical conversion of a biomass particle is essentially treated as a re-

Table 1: Main differences between the present MBM and typical comprehensive MBMs and IBMs.

	Present MBM	Comprehensive MBM	IBM
Hydrodynamic consideration of intra-particle flow	Not considered	Darcy's law or full Navier-Stokes equations	Not considered
Direct resolution of gas-phase species transport inside particle	Not considered	PDEs for each gas-phase species including temporal and spatial gradients, convection and source terms	Not considered
Chemical reaction of gas-phase species inside particle	Not considered	Arrhenius expressions	Not considered
Energy conservation	PDEs for the solid phase	Combined PDEs for both gas and solid phases	ODEs for the temperatures of the solid phase layers and algebraic equations at the boundaries between layers
Solver	Matrix solver (Gaussian elimination by LU factorization)	Matrix solver (Gaussian elimination, e.g. tridiagonal matrix algorithm; possibly with auxiliary algorithms for handling pressure-velocity coupling, e.g. SIMPLE)	ODE solver

active variable-volume one-dimensional transient heat conduction problem. The conceptual basis for the model is a previously developed IBM [5, 6], which has here been fundamentally reformulated in adaptation to the MBM framework. As illustrated in Figure 1, the biomass particle is divided into a number of segments. In a conventional IBM, these segments would be few and correspond to moist wood, dry wood, char and ash. Here, they merely represent a spatial discretization of the particle and they may, at any given point in time, correspond to either of the four previously listed constituents, or a mixture thereof. The basis for the MBM formulation is the treatment of the local particle properties as mass-weighted averages of the four basic constituents, in effect turning the MBM into a "one-solid" model in the vein of "one-fluid" models for segregated multiphase flows.

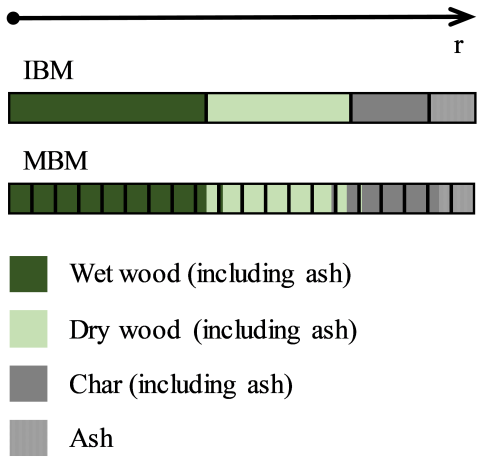

Figure 1: Schematics of one-dimensional MBM.

The governing equation to be solved is thus:

$$m_p c_p \frac{\partial T_s}{\partial t} = \frac{V_p}{\Gamma} \frac{\partial}{\partial r} \left(\Gamma \kappa \frac{\partial T_s}{\partial r} \right) + S_{energy} \tag{1}$$

where m_p is the particle mass (kg), c_p is the particle heat capacity (J/kg K), T_s is the particle temperature (K), t is the time (s), V_p is the particle volume (m^3), Γ is the particle shape factor (m^2), r is the homogenized radial position (m), κ is the particle thermal conductivity (J/m K s) and S_{energy} is the source term (J/s) due to the conversion processes (drying, devolatilization and char combustion). Expressions for the particle shape factor are given in Table 2. Radiative heat transfer inside the particle may be included via a semi-empirical contribution to the particle thermal conductivity [15]. However, this contribution is neglected in the current work, as the process is mostly heat-transfer controlled at lower temperatures (during drying and devolatilization) and mass-transfer controlled during char combustion (when the temperatures are high).

The particle properties in Equation (1) are mass-weighted averages based on the local presence of moist wood, dry wood, char and ash. Equation (1) is discretized using a fully implicit finite-volume method, with a first-order backward differencing scheme for the transient term and a second-order central differencing scheme for the conduction term. The source term linearization ($S_{energy} = S_u + S_p T_s$) uses the temperature at the new time level to harmonize with the implicit treatment, and the discretized equation [22] for the temperature becomes:

$$T_{s,P} = \frac{\chi_W T_{s,W} + \chi_E T_{s,E} + \chi_P^0 T_{s,P}^0 + S_u}{\chi_P^0 + \chi_W + \chi_E - S_p} \tag{2}$$

Table 2: Particle shape factors.

	Γ
Infinite plate[1]	1
Infinite cylinder[1]	$2\pi r$
Sphere	$4\pi r^2$
Finite cylinder[2]	$2\pi(3r^2 + r(l - d))$
Parallelepiped[3]	$24r^2+8r((l_2-l_1)+(l_3-l_1))+2(l_2-l_1)(l_3-l_1)$

[1] For an infinite cylinder, Γ is related to a unit length of the cylinder, and for infinite plates to a unit area.

[2] Initial length l and initial diameter d.

[3] With initial dimensions $l_1 \times l_2 \times l_3$, where l_1 represents the shortest end.

where the coefficients χ (J/K s) and temperatures T_s have subscripts that refer to the east (E), west (W) and cell center (P) positions, and a superscript of 0 refers to the previous time level. The coefficients and all ancillary expressions used in the discretized model are presented in the Appendix A to this paper. The boundary conditions employed are zero gradient (symmetry) at the particle center and a known temperature at the outer particle boundary. The particle surface temperature is obtained from a heat balance where the conductive heat flux into the particle is equated to the external (convective and radiative) heat flux, under the assumption of no heat accumulation at the surface. A uniform temperature field is provided as the initial condition.

The spatial discretization is performed so that the biomass particle is divided into a number of cells of equal initial mass in its radial direction. Once

the coefficients and source terms for all cells have been calculated, a system of algebraic equations can be assembled. By neglecting the temperature-induced variation of the coefficients over the time step, this equation system can thereafter be solved directly by LU factorization with a matrix solver (Meschach [23]). The combined method is stable, owing to its implicit character, and the employment of a first-order temporal scheme minimizes overhead losses due to re-initialization after each fluid flow time step [21]. The limitations in accuracy of the method brought about by the implicit treatment [24] and the further approximation of slowly varying coefficients can be offset by employing a small enough time step. Here, we take advantage of the fact that a CFD simulation of biomass conversion anyhow must include outer loops where the fluid flow solution is advanced in time with the newly updated source terms from the particle conversion sub-model. This iteration between the particle and the fluid level sets an upper limit on the time step for the sub-model, implying that higher-order methods that would allow time steps longer than the time scales on which the fluid flow must be updated are anyway unnecessary.

2.3. Drying, devolatilization and char conversion

Two types of drying models are common in the literature: thermal drying models and kinetic drying models. In this study, a single first-order (SFOR) kinetic model with an Arrhenius type rate expression ($A_{dry} = 5.13 \times 10^{10}$ 1/s and $E_{dry} = 88$ kJ/mol [10, 15]) is chosen in order to guarantee that the temperature field is everywhere differentiable and to improve numerical stability. Some previous studies have suggested that two types of water are present in woody biomass (free and bound water), the evaporation processes of which

should be modeled separately [15] since they may behave differently. However, the determination of free water and bound water contents is nontrivial, requiring complicated analytical methods (e.g. nuclear magnetic resonance scanning). Considering the low availability of the required data and additional uncertainties it may bring, we do not distinguish between free water and bound water in the current model. Previous experimental work has also indicated that the effect of more tightly bound water on the overall drying process is insignificant under conditions relevant to the current applications [25]. Furthermore, the condensation of water vapor inside the particle is also neglected in the current model, but there is nothing in the model formulation that precludes an extension to include this effect in the future.

Devolatilization of biomass is a very complex process involving decomposition of carbonaceous materials into permanent gases, tar, and char. An accurate prediction of this process is usually considered very difficult. The promising multispecies multistep models [26, 27] and structural models (Bio-FLASHCHAIN [28], Bio-CPD [29], and FG-Bio [30]) are simply too expensive to be used in the CFD simulation of large-scale reactors, despite their potentials to predict product distributions over a wide range of temperature. On the other hand, simple and fast-solving SFOR devolatilization models require information of char yield in advance, making their application less reliable. Hence, a competing devolatilization scheme is selected in this study to balance the computational cost, accuracy, and applicability. The formation of light gases, tar and char are described by three competing SFOR reactions ($A_{dev,gas} = 1.11 \times 10^{11}$ 1/s, $E_{dev,gas} = 177$ kJ/mol, $A_{dev,tar} = 9.28 \times 10^{9}$ 1/s, $E_{dev,tar} = 149$ kJ/mol, $A_{dev,char} = 3.05 \times 10^{7}$ 1/s, $E_{dev,char} = 125$ kJ/mol),

respectively, which were derived from conditions close to this study [31, 32]. In addition, the selected kinetic parameters have been successfully applied to simulate conversion of large biomass particles [2, 15]. In the current work, this set of the devolatilization kinetics is used in all simulations to show collective behaviors, as it is typically difficult to find kinetics matching both wood species and devolatilization conditions.

This study aims to develop a model for combustion of biomass in fixed or fluidized beds where a steep temperature gradient exists inside the particle. Therefore, char is assumed to be converted in an infinitely narrow region similar to the method used in a previously developed IBM [5]. The adoption of this assumption in the MBM avoids the requirement of knowing concentrations of gas-phase reactants at every cell inside the particle, thus, greatly reducing the computational cost. The mass source for char during its conversion ($S_{charc,char}$) is given by the following equation:

$$S_{charc,char} = -\left(1-\alpha\right) C_{O2,\infty} \Omega k_{eff} SA_{char} M_c \tag{3}$$

where α is the fraction of oxygen that is consumed by the volatile gases (-), $C_{O2,\infty}$ represents the oxygen concentration in the far field (mol/m^3), Ω is the stoichiometric factor of the char combustion (-), k_{eff} is the effective rate constant estimated by taking both chemical kinetics and mass diffusion into consideration [5, 19] (m/s), SA_{char} is the surface area of the char front (m^2), and MC is the molar mass of carbon (kg/mol). As shown in a previous work [33], conversion of relatively large char particles at high temperature is usually dominated by the oxidation reaction. Therefore, the gasification reactions are not included in this study. Various reaction schemes for modeling

of char conversion have been proposed previously. With the goal of achieving an acceptable balance between accuracy and computational cost, we choose a global scheme [34]. This is an efficient model that has been widely used to simulate combustion of biomass [5, 19, 35, 36, 37, 38, 39]. Moreover, it has been well documented that the external mass transfer is the rate-limiting mechanism for char oxidation in biomass-fueled grate-fired and fluidized-bed furnaces [33, 40, 41], so different kinetic parameters may only have limited effect on the overall conversion process of the char. Since the current single particle model is intended to be coupled with a CFD solver where gas phase reactions are handled, homogeneous gas phase reactions inside the particle are not explicitly calculated. The consumption of oxygen by volatile gases is instead estimated by a factor α:

$$\alpha = \min \left(\frac{-S_{dev,dry\_wood} \left(1 - AC_{dry\_wood}\right) \left(\frac{w_C}{M_C} + \frac{w_H}{4M_H} - \frac{w_O}{2M_O} \right)}{SA_{sur} C_{O2,\infty} \beta} - \frac{S_{dev,char} \left(1 - AC_{char}\right) \frac{1}{M_C}}{SA_{sur} C_{O2,\infty} \beta}, 1 \right) \tag{4}$$

where S_{dev,dry_wood} and $S_{dev,char}$ are mass source terms for dry wood and char during the devolatilization process respectively (kg/s), w_C, w_H, w_O are mass fractions of carbon, hydrogen, and oxygen in the dry wood, respectively (-), AC_{dry_wood} and AC_{char} are ash contents in dry wood and char, respectively (-), M_H and M_O are molar mass of hydrogen and oxygen (kg/mol), SA_{sur} is the particle surface area (m^2), and β is the mass transfer coefficient (m/s). To simplify the estimation, char is considered to contain only carbon and volatile gases are assumed to be converted fully into CO_2 and H_2O.

2.4. Additional model information

Shrinkage is a non-negligible phenomenon accompanying the entire conversion process of a biomass particle including drying, devolatilization, and char conversion. It is influenced by several factors, such as type of biomass, water content, biomass density, size of the particle, and external heating conditions [42]. Given that shrinkage depends on many parameters, it should ideally be measured experimentally at the conditions of interest [43]. Here, the volumetric shrinkage from dry wood to char (SF_{dev}) and from char to ash (SF_{charc}) is estimated by constants (28% and 95%, respectively), as described in a previous study [5]. Shrinkage during drying is calculated based on wood species and moisture content as explained in the literature [42]. It is important that the thermal properties are chosen in a consistent way with regard to the changes the particle undergoes during conversion (mass loss and shrinkage) [44]. This is, however, not a straightforward task particularly for the determination of the thermal conductivity due to the variations in wood species and moisture content. A general equation describing thermal conductivity perpendicular (tangential and radial directions) to the grain [43] was used in this study, whereas the thermal conductivity parallel to the grain was estimated as 1.8 times the value in the perpendicular direction [43]. The overall thermal conductivity was calculated by averaging in all three directions [44]. Regarding the thermal conductivity of char, a wide range of values have been reported with magnitudes (in J/m K s) ranging from 10^{-2} to 10^{0} [2, 3, 15, 19, 43, 44, 45]. Thus, a median value of 0.1 was chosen in this study. Details about the thermal conductivity and other model parameters are listed in Table 3.

Table 3: Model parameters.

Parameter	Expression	Ref.
Specific heat capacity c_p (J/kg K)	wet wood: $(4.206T_s - 37.7)(1 - MC_{wb}) + 4309MC_{wb} + (23.55T_s - 1320MC_{db} - 6191)\,MC_{db}$	[45]
	dry wood: $4.206T_s - 37.7$	[45]
	char: $-119 \times 10^{-12}{T_s}^4 + 1010 \times 10^{-9}{T_s}^3 - 3160 \times 10^{-6}{T_s}^2 + 4410 \times 10^{-3}T_s - 334.0$	[45]
	ash: $754 + 0.586\,(T_s - 273.15)$	[19]
Thermal conductivity κ (J/m K s)	wet wood: $3.8\,(S_g\,(0.1941 + 0.4064MC_{db}) + 0.01864)\,/3$ S_g is the specific gravity	[46]
	dry wood: $3.8\,(0.1941S_g + 0.01864)\,/3$	[46]
	char: 0.1	
	ash: $754 + 0.586\,(T_s - 273.15)$	[19]
Initial density ρ (kg/m^3)	beech: 718 $(MC_{wb} = 20\%)$	[42]
	poplar: 844 $(MC_{wb} = 40\%)$	[42]
	boxwood: 830 $(MC_{wb} = 0\%)$ [1]	[47]
SF_{dry} (-)	beech: 14% $(MC_{wb} = 20\%)$	[42]
	poplar: 13% $(MC_{wb} = 40\%)$	[42]
	boxwood: 0% $(MC_{wb} = 0\%)$ [1]	
Particle emissivity ϵ (-)	0.85	[15]

[1] MC_{wb} is assumed to be zero, as it was not directly stated in the original work [47].

All the simulations were calculated sequentially using one of the computational cores from an Intel® Xeon® X5650 CPU (2.66 GHz, Intel® Turbo Boost Technology disabled, Intel® Hyper-Threading Technology disabled). The overall solving procedures for the IBM and the MBM are outlined in Figure 2.

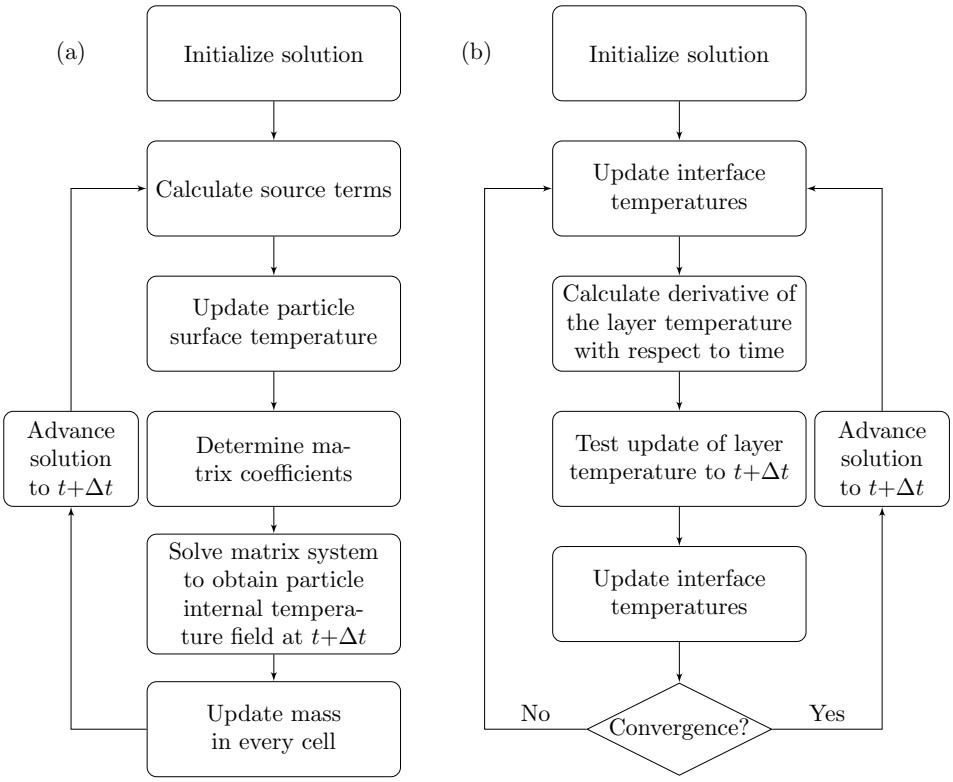

Figure 2: Solving procedures for the MBM proposed in the current work (a) and the IBM on which it is based (b).

3. Model validation

The developed MBM has been validated against experimental data from three different studies [14, 15, 47]. The first experiment is pyrolysis of a

spherical beech particle (d = 0.02 m, MC_{wb} = 20%) in a nitrogen atmosphere at a temperature of 1098 K. The ambient gas temperature (T_g) and reactor wall temperature (T_w) in the simulation was considered to be the same as they were not distinguished in the original study [14]. The second experiment is combustion of a near-spherical poplar particle ($d = 0.0095$ m, $MC_{wb} = 40\%$) in air. The reactor wall temperature and ambient gas temperature were configured as 1050 K and 1273 K, respectively in the simulation according to the experiment [15]. Due to insufficient information provided in the experimental studies, the convective heat transfer coefficient was estimated from a correlation [48]. In both simulations, the particle is discretized into 50 cells. A relatively small time step of 1.0×10^{-4} s was chosen to ensure stability and accuracy of the solution.

In addition to the experimental data, simulation results from other well-validated models were also added. These include three comprehensive MBMs (MBM 1 [14], MBM 2 [17], and MBM 3 [15]) and two IBMs (IBM 1 [5, 6] and IBM 2 [18]) developed focusing on the numerical efficiency. We aim here to illustrate the general performance of the single-particle model with the assumption of constant boundary conditions. It should also be noted that the same property and kinetic parameters were used in IBM 1 and the proposed MBM, so that a direct comparison between the two different modeling philosophies can be made.

The evolutions of particle surface temperature, particle central temperature, and mass loss for pyrolysis of a beech particle are shown in Figure 3. As shown in Figure 3, a good agreement between the model predictions and the experimental data can be found for the evolutions of both temperatures

and mass loss ratios. In general, with thermochemical parameters as listed in Table 3, the proposed MBM is able to reasonably capture both surface temperature and mass loss during pyrolysis of a woody biomass particle. In fact, all the included models behave similarly, despite being constructed in significantly different ways. Nearly identical surface temperature profiles were produced using different models. However, relatively large differences are shown in Figure 3(b) regarding the center temperature. It is however interesting to see that the IBM 1, using a thermal drying model, and the proposed MBM, using a kinetic drying model, predicted very similar drying times (the time until the center temperature rises above the boiling point of water). This further proves the applicability of both models. The difference between model predictions of the drying time mainly stem from the selection of the thermochemical parameters, such as heat capacity and thermal conductivity. Examples of the influence of such parameters are illustrated in Appendix B by varying the thermal conductivity of char. These examples also show that better agreement with experimental data for both the IBM 1 and the proposed MBM can be obtained by choosing different parameter values. Due to the overlapping of drying and devolatilization, the mass loss of the particle is over 80% at the end of drying in all simulations. Therefore, although different center temperatures were obtained after the end of drying as shown in Figure 3(b), mass loss profiles are rather similar, with the exception of the simplified IBM 2 as indicated in Figure 3(c).

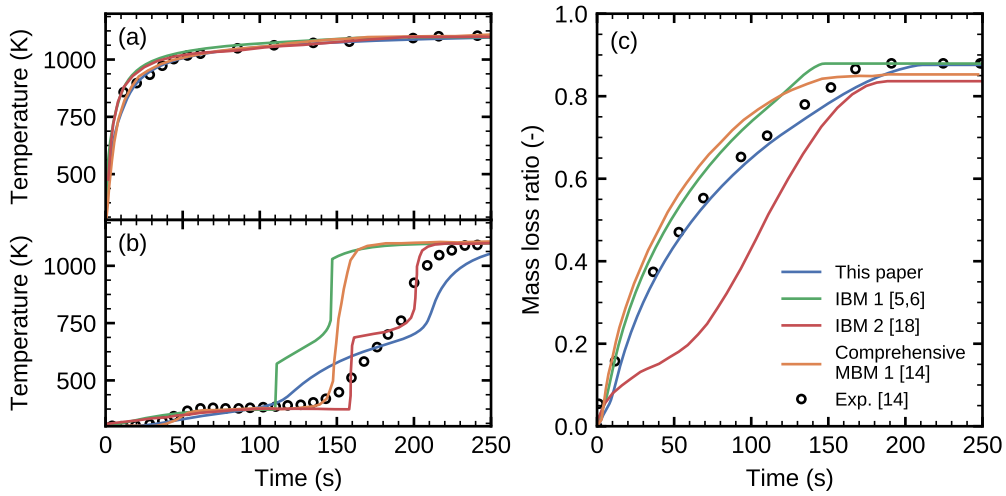

Figure 3: Surface temperature profile (a), center temperature profile (b), and mass loss profile (c) during pyrolysis of a beech particle using the parameters in Table 3. Better agreement for the current MBM and IBM 1 can be obtained with other parameters, as shown in Appendix B. ($d = 20$ mm, $T_w = T_g = 1098$ K, $MC_{wb} = 20\%$, $\phi_{N2} = 100\%$)

Similarly, comparisons between model predictions and experimental data of combustion of a poplar particle are shown in Figure 4. It can be seen in Figure 4(a) that relatively big differences exist between the simulated surface temperatures and the experimental data. All models give over-prediction of the surface temperature at the early stage of the conversion process (less than around 20 s). This disagreement likely arises from the experimental uncertainties, as explained by the authors of the original work [15]. Since the surface temperature was measured by a thermocouple buried next to the surface, the reading from the thermocouple might be slightly lower than the actual value. All models underpredict surface temperatures after around 10–20 s. The lack of heat flux from the volatile flame perhaps contributes most to the underprediction of the surface temperature. Unfortunately, it is difficult to

accurately describe the process of volatile combustion using a single-particle model only. This issue, however, can be resolved by the coupling with a CFD solver. Additionally, authors of the experimental work have stated that the bead of the thermocouple might lose contact to the particle surface and expose to the volatile flame during the tests [15], which potentially resulted in higher temperature readings. It should be noted that the surface temperature calculated from the proposed MBM decreases slightly at around 50 s as shown in Figure 4(a), which is a result of the completion of the drying process. If a particle contains moisture, the center temperature of the particle stays relatively low. The devolatilization front moves gradually from the hot surface to the cold drying front, thus gently releasing volatile gases. A small amount of volatile gases does not consume all the oxygen transported to the particle surface. Therefore, there is still oxygen left for the exothermic char oxidation, which elevates the particle surface temperature. However, after the depletion of moisture inside the particle, the temperature of the particle increases dramatically. A large amount of volatile gases is released accordingly, and this causes a complete consumption of the oxygen that terminates further char oxidation temporarily. Without the heat released from char oxidation, the surface temperature decreases slightly. Again, despite the large differences between measured and calculated temperatures, the mass loss ratios predicted by all models (apart from the IBM 2) agree well with the experiment as shown in Figure 4(c). This phenomenon is further discussed in Section 4.

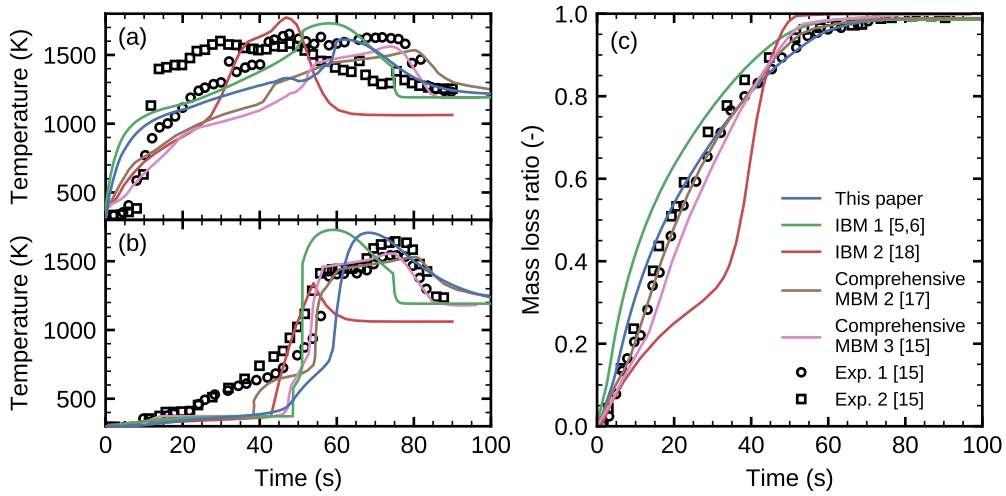

Figure 4: Surface temperature profile (a), center temperature profile (b), and mass loss profile (c) during combustion of a poplar particle. ($d = 9.5$ mm, $T_w = 1273$ K, $T_g = 1050$ K, $MC_{wb} = 40\%$, $\phi_{O2} = 21\%$, $\phi_{N2} = 79\%$)

It can be seen from Figure 4(b) that all models produced a distinct temperature plateau until around 40–50 s owing to the drying process. In fact, it is promising to see that all models predict a similar drying time. On the other hand, the measured temperature rises gradually after only 10 s. Such behavior may be caused by heat conduction along the wire as detailed in a recent study [47]. This influence should be more severe in the combustion case [15] than in the pyrolysis case [14] due to the smaller particle and higher gas temperature. In order to further test the proposed MBM under such conditions (small particle and high gas temperature), another experiment [47] was used for validation, which contains measured temperature profiles for pyrolysis of boxwood particles with three different diameters ($d = 0.003,\ 0.005,\ 0.008$ m). In the simulation, the ambient gas temperature was set to 1355 K, which is same as the measured gas temperature at the end of the experiment (50

s after the start of the experiment), whereas the reactor wall temperature was set to 723 K, as given in the experimental work [47]. Figure 5 shows the comparison between measured center temperature and calculated values using the proposed MBM. Note that all the shown experimental data have been corrected to minimize the effect of heat conducted along the thermocouple wires [47]. It is clear that a better agreement is achieved compared to Figure 4(b).

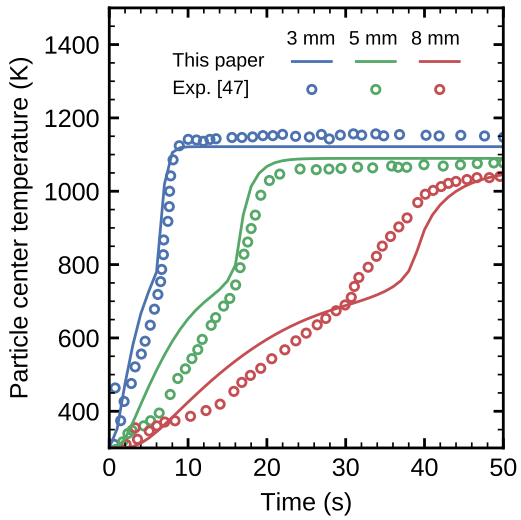

Figure 5: Center temperature profile during pyrolysis of boxwood particles using the parameters in Table 3. (d = 3, 5, 8 mm, T_w = 723 K, T_g = 1355 K, MC_{wb} = 0%, ϕ_{N2} = 100%)

4. Results and discussion

In order to better understand the effects of spatial and temporal resolution on the performance of the MBM, the two validation cases described in Section 3 (the pyrolysis of a 20 mm beech particle and the combustion of a 9.5

mm poplar particle) were investigated further. The influence of the spatial resolution of the MBM was investigated by varying the numbers of cells, and the influence of the temporal resolution was studied by changing the time step. In addition, two non-dimensional factors, relative error (RE, %) and relative calculation time (RCT, -), are defined accordingly as:

$$RE = 50\%\sqrt{\frac{1}{n}\sum_{t=1,2,\ldots,n}^{n=\lfloor t_{total,con} \rfloor}\left(\frac{m_p(t) - m_{p,BL}(t)}{m_{p,BL}(t)}\right)^2} + 50\%\sqrt{\frac{1}{n}\sum_{t=1,2,\ldots,n}^{n=\lfloor t_{total,con} \rfloor}\left(\frac{T_{s,sur}(t) - T_{s,sur,BL}(t)}{T_{s,sur,BL}(t)}\right)^2} \tag{5}$$

$$RCT = \frac{t_{total,cal}}{t_{total,con}} \tag{6}$$

where $m_p(t)$ and $m_{p,BL}(t)$ are the particle masses (kg) calculated from a test case and a baseline case at time t respectively, $T_{s,sur}(t)$ and $T_{s,sur,BL}(t)$ are the particle surface temperatures (K) calculated from a test case and a baseline case at time t, respectively, $t_{total,con}$ is the total conversion time of a particle (s), and $t_{total,cal}$ is the elapsed real time (wall-clock time) for the calculation (s). When coupled with a CFD solver, the MBM exchanges energy and mass with the surrounding environment. Accurate estimations of surface temperature and mass loss of the particle are crucial to calculate fluxes of energy and mass coming out of the MBM. Therefore, a combined error function defined by both surface temperature and mass of the particle is constructed in Equation (5). The baseline case referred to is a case configured with very fine spatial and temporal resolutions. Details are given in the following sections.

4.1. Effect of the spatial resolution

Figure 6 shows predicted temperatures and mass loss ratios during combustion of a 9.5 mm poplar particle using the MBM with the same time step of 1×10^{-4} s but different degrees of spatial discretization (i.e. different numbers of cells). Note that the case denoted as $10^{\dagger}$ was configured slightly different from the others, in that combustion of char was not allowed until all the dry wood in the particle had become char. The surface temperature profiles look overall similar in Figure 6(a). However, some oscillations can be observed for the cases with coarse spatial resolution. These oscillations are caused by intermittent char conversion in the outermost cell. Since the volatile flame is not accounted for in the particle model when de-coupled from a CFD solver, the available oxygen for char conversion is instead estimated from the amount of hydrogen being released (cf. Section 2.3). As indicated from the surface temperature of the $10^{\dagger}$ case before 50 s, the outermost cell was heated to a high temperature even without char conversion. This situation makes the char conversion in this cell very sensitive to the available oxygen concentration. Given the small thermal mass of this cell, even a small amount of oxygen can cause a big increase in the local temperature, and consequently also in the surface temperature. Similar oscillating behavior has also been reported previously using a different particle model [49]. Although the oscillation may appear dramatic, its influence on the overall particle conversion is nearly negligible as shown in Figure 6(c). Moreover, this oscillating phenomenon would be greatly reduced in a CFD simulation of a large furnace, in which the oxygen concentration is influenced by a collective of particles and the homogenous gas phase combustion is simultaneously

accounted for.

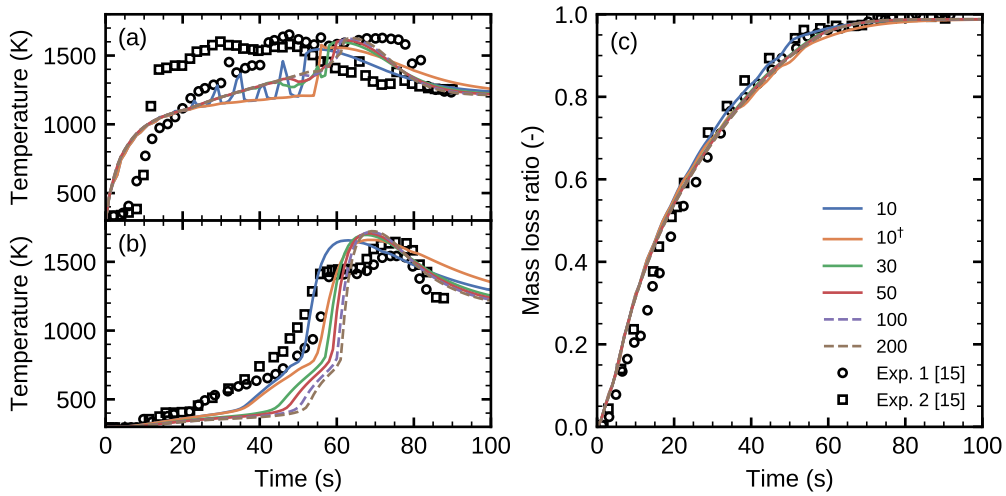

Figure 6: Effect of the spatial resolution on surface temperature profile (a), center temperature profile (b), and particle mass loss ratio (c) during combustion of a poplar particle. ($d = 9.5$ mm, $T_w = 1273$ K, $T_g = 1050$ K, $MC_{wb} = 40\%$, $\phi_{O2} = 21\%$, $\phi_{N2} = 79\%$)

With an increased degree of spatial resolution, calculated surface temperatures seem to converge to the same values. On the other hand, the particle center temperature varies more with the number of cells. This is due to that the center temperature shown in Figure 6(b) is in fact the temperature of the innermost cell. Since the particle is heated externally, the larger the inner cell is (i.e. the lower the degree of spatial discretization is), the sooner the center temperature appears to rise inside the particle. As shown in Figure 6(c), the effects of spatial resolution on the mass loss ratio are very small: the predicted mass loss evolution is well characterized already at a resolution of 10 cells.

Both temperature and heating rate may affect product distribution during the devolatilization process. As shown in Figure 6, certain variations can

be observed in the temperature prediction with varying degrees of spatial discretization. Since competing reactions have been implemented for resolving the devolatilization process, the spatial discretization may also have an influence on the distribution of the devolatilization products. Figure 7 shows the normalized cumulated mass for gas, tar, and char under the same condition as used in Figure 6 as obtained with particle resolutions of 10, 50, and 200 cells. It seems that nearly identical product distributions are obtained. The heating rate of the particle is relatively low (estimated to be below 100 K/s during the devolatilization process) under the tested condition, and the slight differences in the temperature prediction caused by varying spatial resolution are too small to influence the product distribution.

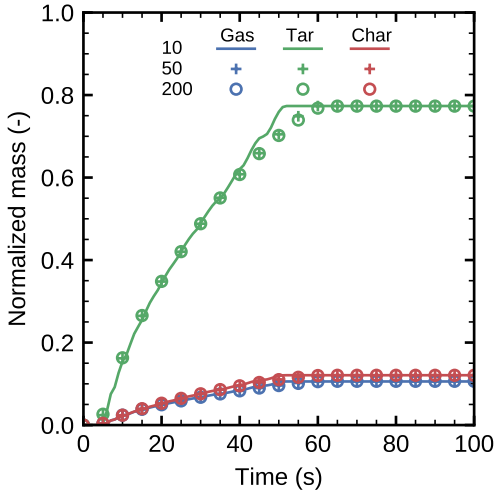

Figure 7: Effect of the spatial resolution on distribution of the devolatilization products during combustion of a poplar particle. The product mass is normalized by the initial particle dry mass. ($d = 9.5$ mm, $T_w = 1273$ K, $T_g = 1050$ K, $MC_{wb} = 40\%$, $\phi_{O2} = 21\%$, $\phi_{N2} = 79\%$)

By using Equations (5) and (6), quantitative differences of computational

accuracy and cost between calculations with various degrees of discretization were obtained, as shown in Figure 8. Besides the combustion test case, the pyrolysis of a 20 mm particle described in Section 3 was also simulated. The relative errors shown in Figure 8 were calculated by comparing with the baseline cases, respectively for the combustion (200-cell spatial discretization) and pyrolysis (300-cell spatial discretization) conditions. The low relative errors again demonstrate that the predictability of MBM model is not sensitive to the spatial resolution at the tested conditions. On the contrary, the calculation time is heavily influenced by the number of cells (note a logarithmic scale is used). It can be estimated from Figure 8 that when the number of cells is lower than 25, the RCT is lower than 1 or, in other words, the time used for executing the code is shorter than the actual physical conversion process simulated.

The computational efficiency of the MBM is further analyzed by timing different operations, i.e. solving the matrix system and all other operations. The effect of the spatial resolution on the time used for the matrix solver and the other operations are shown in Figure 9. As described in Section 2.2, the system of linear equations is directly solved by LU factorization to obtain the temperature of each discretized cell. The computational cost of solving such a system scales with the size of the system to the power of three. Consequently, as shown in Figure 9, the time used for solving matrix is almost proportional to cube of the number of cells. The rest of the operations, such as calculations of the reaction rates and updating the mass, need to be performed the same number of times for each individual cell at any given time. Therefore, the time used for those operations is linearly correlated to the number of cells.

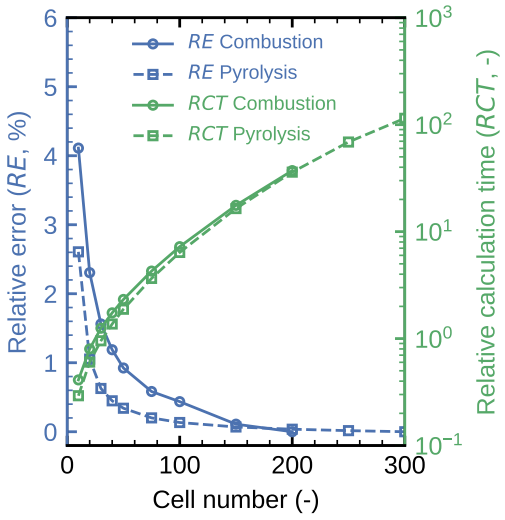

Figure 8: Effect of the spatial resolution on relative error and relative calculation time. (combustion: poplar, $d = 9.5$ mm, $T_w = 1273$ K, $T_g = 1050$ K, $MC_{wb} = 40\%$, $\phi_{O2} = 21\%$, $\phi_{N2} = 79\%$; pyrolysis: beech, $d = 20$ mm, $T_w = T_g = 1098$ K, $MC_{wb} = 20\%$, $\phi_{N2} = 100\%$)

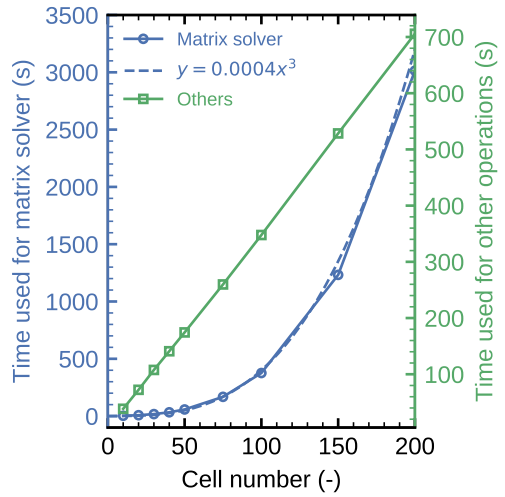

Figure 9: Effect of the spatial resolution on computational efficiency. (poplar, $d = 9.5$ mm, $T_w = 1273$ K, $T_g = 1050$ K, $MC_{wb} = 40\%$, $\phi_{O2} = 21\%$, $\phi_{N2} = 79\%$)

4.2. Effect of the temporal resolution

Figure 10 shows the effect of the temporal resolution (time step) on the prediction of temperature and mass loss using the MBM. The same condition of the combustion of a 9.5 mm poplar particle was used. All the calculations shown in Figure 10 were obtained using the same spatial discretization of 50 cells, which is sufficient to obtain reasonable results under the tested conditions as illustrated in Section 4.1. As shown in Figure 10, most of the profiles look nearly identical, except the ones calculated with time steps larger than 1×10^{-2} s. Since a fully implicit finite-volume method is used in the MBM, an unconditionally stable solution should be expected. However, as mentioned before, solutions calculated with time steps larger than 1×10^{-2} s differ significantly to other results. This suggests that some physical processes limit the largest tolerable time step with respect to solution accuracy. Detailed illustrations of this phenomenon are given in the next section.

The effect of the temporal resolution on computational accuracy and cost for both combustion and pyrolysis conditions are shown in Figure 11. It is not surprising that the computational cost is inversely proportional to the time step. When the time step is larger than 5×10^{-4} s, the computational time is shorter than the physical conversion time at the tested conditions and current spatial discretization. The relative errors were estimated by comparing to the base cases calculated with a time step of 1×10^{-5} s. For both tested combustion and pyrolysis conditions, a very small relative error can be obtained by using a time step smaller than 1×10^{-2} s.

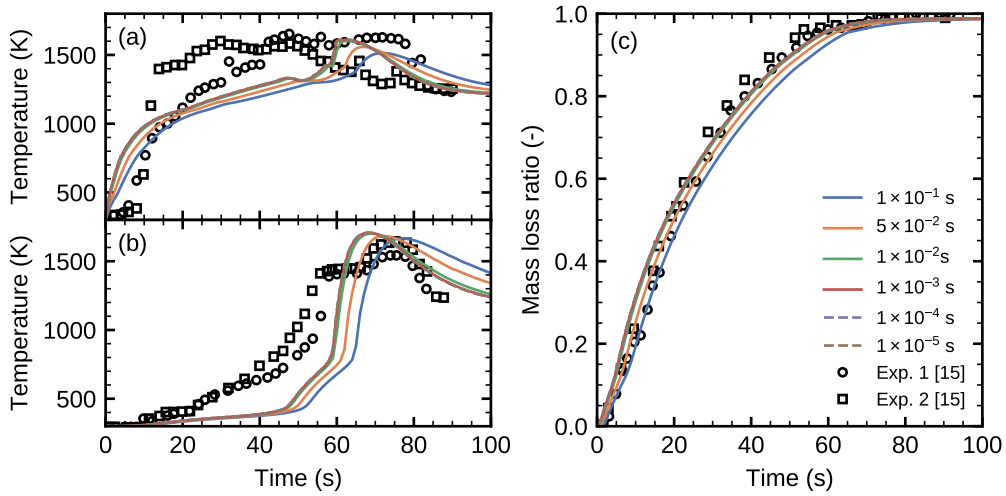

Figure 10: Effect of the temporal resolution on surface temperature profile (a), center temperature profile (b), and particle mass loss ratio (c) during combustion of a poplar particle. ($d = 9.5$ mm, $T_w = 1273$ K, $T_g = 1050$ K, $MC_{wb} = 40\%$, $\phi_{O2} = 21\%$, $\phi_{N2} = 79\%$)

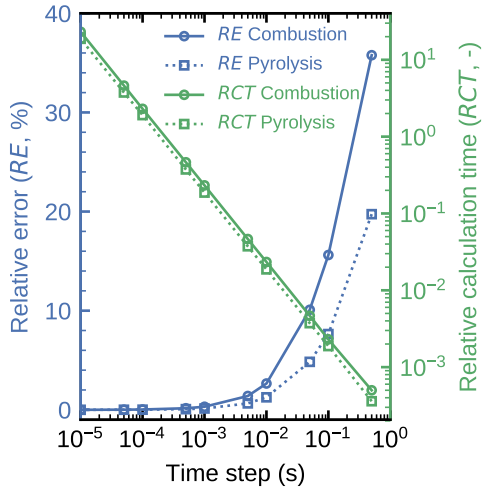

Figure 11: Effect of the temporal resolution on relative error and relative calculation time. (combustion: poplar, $d = 9.5$ mm, $T_w = 1273$ K, $T_g = 1050$ K, $MC_{wb} = 40\%$, $\phi_{O2} = 21\%$, $\phi_{N2} = 79\%$; pyrolysis: beech, $d = 20$ mm, $T_w = T_g = 1098$ K, $MC_{wb} = 20\%$, $\phi_{N2} = 100\%$)

4.3. Optimal spatial and temporal resolutions

Despite the unconditionally stable nature of the implicit scheme used to solve Equation (1), small time steps are required to ensure accuracy. In order to find the optimal spatial and temporal resolutions, three scenarios (inert heating, pyrolysis, and combustion) were tested based on the condition of the combustion of a 9.5 mm poplar particle described in the previous sections. The drying, pyrolysis, and char conversion were disabled in the inert heating cases, whereas the char conversion was turned off in the pyrolysis cases. The surface temperature profiles for the inert heating scenario with various level of spatial and temporal resolutions are shown in Figure 12.

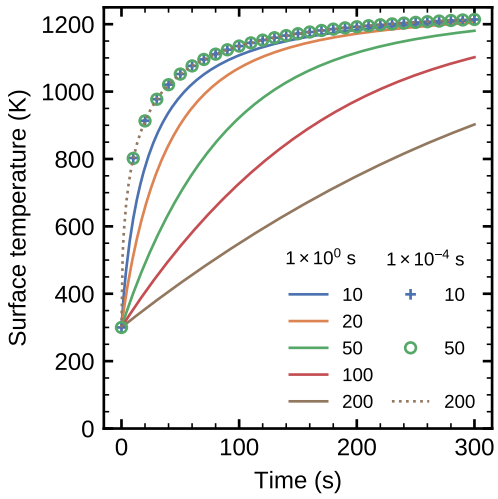

Figure 12: Effect of spatial (cells: 10 – 200) and temporal resolutions (time step: 1×10^0 and 1×10^{-4} s) on prediction of surface temperature during heat transport process.

As shown in Figure 12, when the time step is small (1×10^{-4} s), the obtained surface temperatures are identical for the cases with varying spatial resolutions. Due to the similarity, only three cases were plotted. However,

large discrepancies can be noted from the cases calculated using the time step of 1×10^0 s. Counterintuitively, the results deviate more with an increased number of grid points. This observed phenomenon can be attributed to the comparison between the time step and the time scale of conductive heat transfer (t_{HT}) inside the particle, which is defined by the equation below:

$$t_{HT} = \frac{(\text{length scale})^2}{\text{thermal diffusivity}} \tag{7}$$

The length scale of each discrete volume can be estimated by the distance between two adjacent grid points. Therefore, when the particle size remains constant, this length scale reduces as the number of grid points increases, and so does the associated time scale t_{HT} for cell-to-cell heat conduction. If t_{HT} is smaller than the time step used in the solution procedure, the heat transfer process cannot be resolved accurately. Figure 13 shows the heat transfer timescale of each discretized cell for all three scenarios (time step = 1×10^{-4} s and cell count = 50). The heat transfer time scales for all cells increase initially due to the decreasing thermal diffusivity when temperature is elevated. Since the spatial discretization is performed by dividing the particle into equal mass cells (i.e. equal volume cells) in its radial direction, the length scale of the cell decreases from particle center to particle surface. For the inert heating case shown in Figure 13(a), it is apparent that majority of the timescales are smaller than 1×10^0 s. Consequently, a large deviation can be found for the results calculated using the time step of 1×10^0 s and the spatial discretization of 50. As the cell number increases, even smaller time steps are required, and thus more severe underprediction of the surface temperatures were obtained as shown in Figure 12.

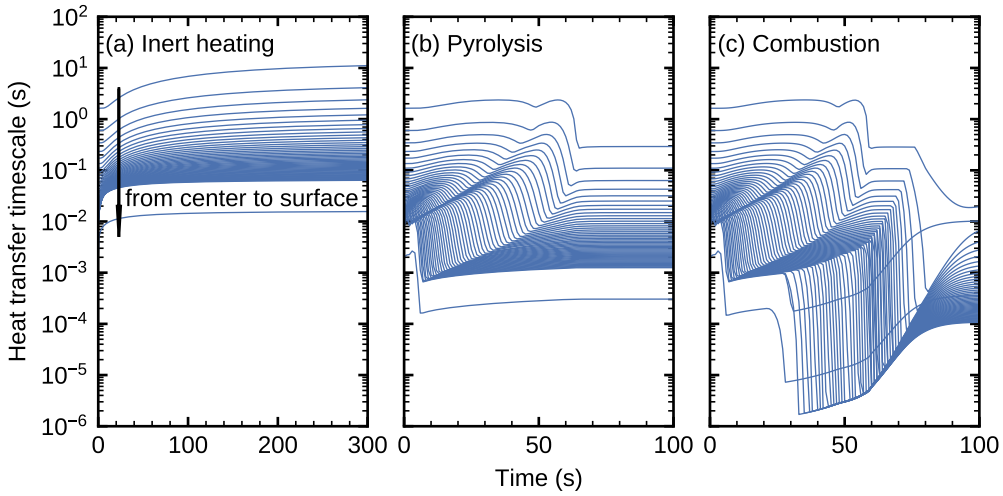

Figure 13: Heat transfer time scale of each cell during inert heating (a), pyrolysis (b), and combustion (c). ($d = 9.5$ mm, $MC_{wb} = 40\%$, $T_w = 1273$ K, $T_g = 1050$ K)

Due to the reduction of the computational cell size caused by the phase change and chemical reactions, significant reduction in the time scales can be observed for the pyrolysis and combustion cases in Figure 13(b) and 13(c), respectively. This reduction is particularly pronounced for the combustion case because of the severe shrinkage and mass loss during the char conversion process. In fact, the size of the outmost layer needs to be kept constant during the char conversion process to improve the stability of the MBM model. To better assess the effect of phase change and chemical reaction on the choice of time step and spatial discretization, REs were calculated for both pyrolysis and combustion scenarios using two baseline cases (time step of 1×10^{-5} s and spatial resolution of 200 cells). The results are shown in Figure 14.

Interestingly, although the absolute values are different, similar trends can be observed for the pyrolysis and combustion cases. Nearly identical

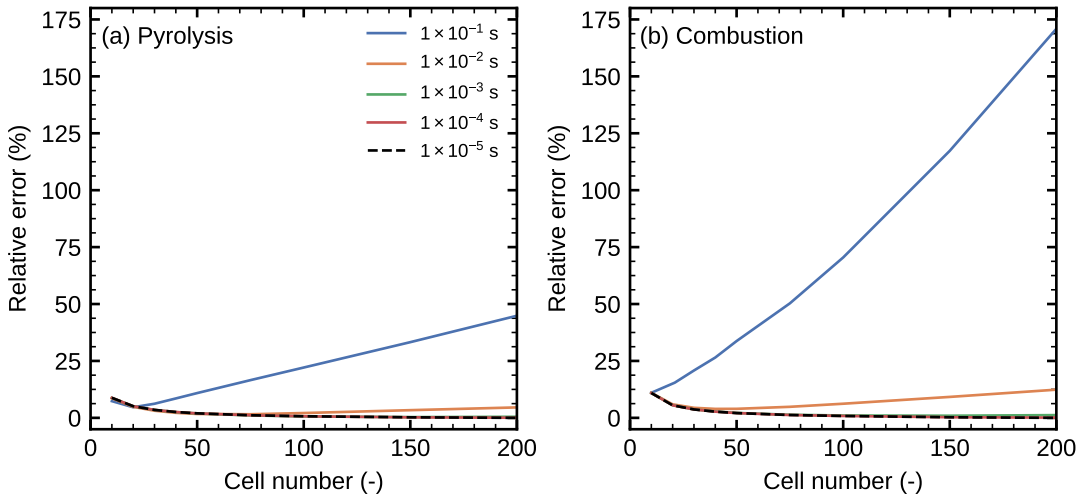

Figure 14: Comparison of computational accuracy between pyrolysis (a) and combustion (b) cases.

results are obtained when the time step is smaller than 1×10^{-4} s, regardless of spatial resolutions for two conditions. However, as shown in Figure 13, big differences of t_{HT} exist between the combustion and pyrolysis cases. This apparent contradiction may be explained by Equation (1). As shown in the right-hand side of Equation (1), both the conductive heat transfer and the explicit energy sources due to drying, devolatilization, and char combustion can influence the solution. To capture the process of biomass conversion, the maximum allowed time step in the simulation should be smaller or at least comparable to the time scales associated with the physical processes described by the MBM. Irrespective of whether t_{HT} is the smallest time scale or not during the conversion process, the time step should at least always be smaller than this time scale to ensure an accurate prediction. The underprediction of the heat transfer caused by using time steps larger than t_{HT} can

have a cumulative effect on the temperature prediction and thus significantly influence the results. On the other hand, both drying and devolatilization are calculated using temperature dependent Arrhenius equations, and devolatilization is typically considered not to be exothermic. Since each layer is gradually heated up from room temperature (or relatively low temperature) through conductive heat transfer during drying and devolatilization, the rates of drying and devolatilization are controlled by the heat transfer process. The point to have a time step smaller than a time scale of a certain process is to be able to well resolve the changes of that process. The change of the rate for drying or devolatilization is the result of changing temperature (assuming the process is not limited by the available mass). Due to the nature of the non-positive feedback from drying and devolatilization on temperature, even if the time step is larger than the time scales of those two processes, a fairly accurate temperature prediction can be obtained assuming the conductive heat transfer is well accounted for. Therefore, it is important to have a time step that is smaller than the t_{HT} in most of the cells before completion of devolatilization.

It should be noted that, in contrast to drying and devolatilization, char conversion releases heat, which provides a positive feedback on temperature. This situation implies to a certain restriction on the time step. In the meantime, since the conductive heat flux is likely to be much smaller than the heat released from the exothermic char oxidation reaction, an accurate prediction of the conductive heat transfer becomes less crucial. Nevertheless, as shown in Figure 11 and Figure 13(c), the analysis on t_{HT} fits well with the results. This indicates that such a time step also fulfills the requirement

for the char conversion under the tested conditions, perhaps because of the limited oxygen availability.

4.4. Applications to industrial conditions

Two common industrial applications (grate furnaces and fluidized-bed furnaces) are taken as examples in this section to provide a guideline for choosing the optimal parameters (cell number and time step) for the MBM. Typically, wood chips and briquettes are used in the biomass-fired grate furnaces, which are in the size range of 10^1 to 10^2 mm, whereas, smaller sized chips and pellets are usually utilized in the fluidized-bed furnaces (<80 mm for bubbling fluidized-bed and <40 mm for circulating fluidized-bed) [50]. Due to the concerns of ash melting, fluidized-bed furnaces operate at lower temperatures (923—1173 K) than grate furnaces (operating at 1273—1373 K). As shown in Table 4, combustion of a single particle was tested under two conditions resembling environments in grate furnaces and fluidized-bed furnaces, respectively. Two different moisture contents, 5% and 40%, were also studied to cover most common fuel types. The model parameters for the MBM were chosen in the context of CFD simulations. Because of the high computational cost for large-scale reactive CFD simulations, Reynolds-averaged Navier–Stokes based turbulence models are usually used to simulate industrial furnaces. The time step used in such simulations is in the order of 10^{-3} s. If the MBM is employed as a particle conversion sub-model in a CFD simulation, time step of the MBM should not be larger than time step of the fluid solver. Therefore, a time step of 1×10^{-3} s was selected in the following test cases. As shown in the previous section, the choice of spatial resolution for the MBM has a big influence on the computational cost. To

Table 4: Simulation conditions resembling industrial furnaces.

Grate-fired furnace
d = 50 mm, T_w = T_g = 1323 K,
ϕ_{O2} = 21%, ϕ_{N2} = 79% MC_{wb} = 5
% and 40%
Fluidized-bed furnace
d = 20 mm, T_w = T_g = 1073 K,
ϕ_{O2} = 21%, ϕ_{N2} = 79% MC_{wb} = 5
% and 40%

ensure a good balance between accuracy and cost, a spatial discretization of 20 cells is chosen. This resolution produced a relative error of around 5% in the previous test cases and is in line with the resolutions employed in conventional mesh-based models [14]. A baseline case with a finer resolution (200 cells) and a shorter time step (1×10^{-4} s) was also tested for comparison. Due to the long conversion time required for a full conversion of particle, the simulation was stopped at 95% mass loss.

Simulation results obtained with two sets of model parameters are shown in Figure 15. The computational efficiency (RCT) achieved was nearly identical with the same model parameters, regardless of the particle size, moisture contents and combustion conditions. The proposed time step and grid number yielded satisfactory fast solutions in all tested conditions. Less than 5% error was observed for the majority of the tested cases. The deviation becomes somewhat larger towards to the end of the conversion, but remains

within an acceptable level. On average, around 400 times speedup could be achieved when compared to the baseline cases. Considering the outdated CPU (launched in 2010) used, the *RCT* could be further reduced to a large degree by using modern computational architectures.

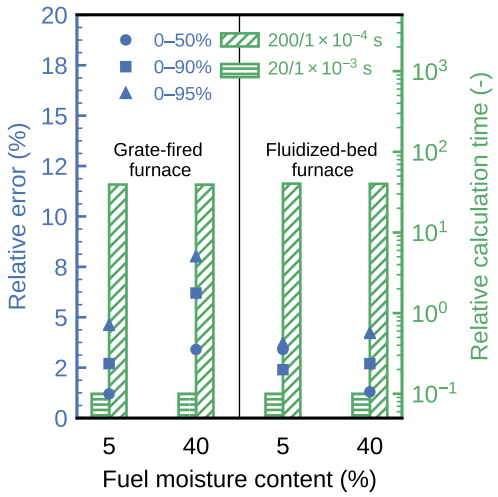

Figure 15: Comparison between simulations of biomass conversion under industrial conditions with different model parameters. Relative errors up to 50%, 90%, and 95% of mass loss are calculated by comparing with the baseline simulation.

Finally, the computational overhead of the MBM is evaluated in a test run with the fixed-bed combustion model described in a recent study [51]. These simulations are designed to simulate the combustion of wood pellets loaded in a 60 L bench-scale fixed-bed reactor. In this test run, the bed is discretized in 100 computational cells in the vertical direction and the CFD model is based on the three-dimensional transient pressure-based segregated solver using operator splitting available in ANSYS Fluent 15.0.7. When the herein presented MBM is employed as the sub-model for the particle phase (cell number 20 and time step 1×10^{-3} s) at a CFD time step of 1×10^{-3} s,

the computational overhead is only a mere 2.2%. We thus conclude that the MBM, used under such conditions, is not the limiting factor with regard to the overall computational efficiency of the combined framework.

The most important implication of the current work is thus that the particle model opens up for new approaches to treating large ensembles of biomass particles. When the cost of solving the particle sub-model is no longer the limiting factor in the computational setup, more instances of particle sub-models can be afforded without significantly increasing the total cost of the simulation. Here, one could envision different scenarios: in one the model would be employed as the basis for a Lagrangian CFD simulation (as in Eulerian-Lagrangian or CFD-DEM approaches), where each particle physically present is represented as one computational particle; in another the model would be used as an Eulerian model of a representative particle in each computational cell to compute the local source terms of all particles (or fractions thereof) present in the CFD-cell in question. In the former approach the particle motion is typically obtained by solving Newton's second law of motion with an auxiliary ODE-solver for each physical particle, whereas in the latter approach such motion is more often prescribed or solved on the same computational mesh used for the gas-phase calculations (e.g. using a continuum model for granular flow as a viscoplastic fluid [52]). The Eulerian approach is particularly attractive with the current sub-model, as it would open up possibilities for dynamic mesh refinement. Regions with small gradients in the solid phase properties could use a coarser resolution, whereas a region of finer mesh resolution would dynamically move with e.g. the combustion front in a fixed-bed reactor (during steady-state operation

of a typical fixed-bed incinerator, the regions of finer resolution would stay in place). Dynamic mesh refinement is only computationally tractable if the coarse and fine regions require significantly different resolution and the cost of re-meshing can be tolerated; the design and performance of the herein proposed particle sub-model, in conjunction with the layout of typical fixed-bed furnaces, imply that these criteria are fulfilled. Furthermore, the low computational cost — and the potential to reduce it even further by dynamic mesh refinement — also mean that several instances of the model could be used in parallel in every computational cell to account for polydispersity in terms of sizes, shapes or even biomass types. Finally, the proposed model is also well suited for massively parallelized high-performance computing platforms. Dynamic load balancing is already a standard feature in most Lagrangian particle models in commercial CFD codes, and in Eulerian frameworks the rules for dynamic load balancing can typically be adjusted via model-based weighting. Unlike IBMs, where dynamic time stepping results in varying computational cost over the lifetime of a fuel particle, the current MBM uses a fixed time step, which simplifies load balancing significantly by making it easier to predict computational costs *a priori*. In conclusion, we believe that it is these new possibilities offered by the robustness and efficiency of the currently proposed model that are most interesting in terms of potential for future applications and development.

5. Conclusion

A mesh-based particle model has been developed with the intention of coupling with CFD solvers. The model was validated against experimen-

tal data from the literature [14, 15] under both pyrolysis and combustion conditions. Using various degrees of spatial and temporal discretization, we demonstrated that the model behaved robustly. Different from most of the existing mesh-based models, the intraparticle flow is not considered in the current model, which enables a good balance between accuracy and computational efficiency. By carefully examining the timescale of conductive heat transfer under conditions of inert heating, pyrolysis, and combustion, we found that the conductive heat transfer plays an important role in the drying and devolatilization processes. Therefore, the time step used in the proposed model should be smaller or at least close to the timescale of conductive heat transfer during the drying and devolatilization processes to obtain a satisfactory simulation of biomass conversion. On the other hand, the highly exothermic process of char conversion is dominated by the transport of oxygen, which is less sensitive to the heat transfer process.

In addition, the model was tested for conversion of a biomass particle under typical conditions in grate-fired and fluidized-bed furnaces. The findings suggested that a resolution of 20 cells per particle at a time step of 1×10^{-3} s is sufficient for a reliable prediction of biomass conversion. The execution time for the model was around only one tenth of the physical conversion time. To further assess the computational efficiency, the model was implemented into a CFD solver. The simulation of a bench-scale fixed-bed reactor showed that the model introduced merely 2.2% additional computational overhead to the cost of solving for the reactive gas flow through the bed. Further investigation with larger-scale CFD simulation would be useful to show the full potential of the model. When used as a sub-model in Eulerian simulations of

fixed-bed conversion, the exhibited computational performance is sufficient to open up opportunities for handling fuel polydispersity and/or dynamic mesh refinement.

Acknowledgments

This work has been financially supported by GASPRO — Fundamental insight into biomass gasification using experiments and mathematical modelling, a researcher project funded by the Research Council of Norway (267916), and CECOST (the Centre for Combustion Science and Technology) and SFC (the Swedish Centre for Biomass Gasification).

Appendix A

In this section, implementation details are illustrated. The particle is first discretized into a given number (Np) of cells of equal mass in one homogenized dimension as shown in Figure A.1.

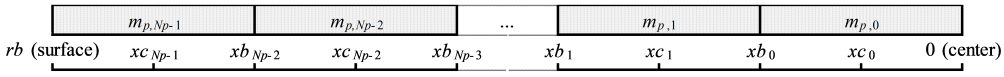

Figure A.1: Schematics of the one-dimensional discretization. xb is the location of the outer cell boundary (m), xc is the location of the cell mass center (m), rb is the radius of the particle (m).

At the beginning of each time step, the mass fraction of each solid species in each cell is first obtained as:

$$w_{wet\_wood} = \frac{m_{wet\_wood}}{m_p} \tag{A.1}$$

$$w_{dry\_wood} = \frac{m_{dry\_wood}}{m_p} \tag{A.2}$$

$$w_{char} = \frac{m_{char}}{m_p} \tag{A.3}$$

$$w_{ash} = \frac{m_{ash}}{m_p} \tag{A.4}$$

where w_{wet_wood}, w_{dry_wood}, w_{char}, and w_{ash} are mass fractions of wet wood, dry wood, char, and ash, respectively (-); m_{wet_wood}, m_{dry_wood}, m_{char}, and m_{ash} are masses of wet wood, dry wood, char, respectively (kg). Afterwards, the volume of the cell (V_c, m^3) is updated by:

$$V_c = V_{wet\_wood} + V_{dry\_wood} + V_{char} + V_{ash} \tag{A.5}$$

where V_{wet_wood}d, V_{dry_wood}, V_{char_wood}, and V_{ash} are volumes of wet wood, dry wood, char, and ash, respectively (m^3), expressed as:

$$V_{wet\_wood} = V^0_{wet\_wood} + \frac{S^0_{dry,wet\_wood}dt}{\rho_{wet\_wood}} \tag{A.6}$$

$$V_{dry\_wood} = V^0_{dry\_wood} + \frac{S^0_{dev,dry\_wood}dt}{\rho_{dry\_wood}} - \frac{SF_{dry}S^0_{dry,wet\_wood}dt}{\rho_{wet\_wood}} \tag{A.7}$$

$$V_{char} = V^0_{char} + \frac{S^0_{charc,char}dt}{V^0_{char}/m^0_{char}} + \frac{SF_{dev}S^0_{dev,char}dt}{\rho_{dry\_wood}} \tag{A.8}$$

$$V_{ash} = V^0_{ash} - \frac{SF_{charc}S^0_{charc,char}dt}{V^0_{char}/m^0_{char}} \tag{A.9}$$

where S_{dry,wet_wood}, S_{dev,dry_wood}, $S_{dev,char}$, and $S_{charc,char}$ are mass sources for wet wood due to drying, dry wood due to devolatilization, char due to devolatilization, char due to char conversion, respectively (kg/s); SF_{dry}, SF_{dev}, and SF_{charc} are shrinkage factors for drying, devolatilization, and char conversion, respectively (-); dt is time step (s); the superscript 0 represents values in the previous time step. After the volume has been updated, the location of each grid point (xc) and the radius of the particle (rb) are then calculated. Depending on the shape factor Γ, different formulations for these updates are used. As an example, for a spherical particle, xc and rb are calculated by:

$$xc_i = \begin{cases} \sqrt[3]{\frac{3}{8\pi} V_{c,i}} & i = 0, \text{ innermost cell} \\ \sqrt[3]{\frac{3}{4\pi} \left(\sum_{j=0}^{i-1} V_{c,j} + \frac{V_{c,i}}{2} \right)} & 0 < i \leq Np - 1 \end{cases} \tag{A.10}$$

$$rb = \sqrt[3]{\frac{3}{4\pi} \sum_{i=0}^{Np-1} V_{c,i}} \tag{A.11}$$

The mass source terms are then updated as:

$$S_{dry,wet\_wood} = -m_{wet\_wood} A_{dry} \exp\left(\frac{E_{dry}}{RT_s}\right) \tag{A.12}$$

$$S_{dev,gas} = m_{dry\_wood} A_{devo,gas} \exp\left(\frac{E_{dev,gas}}{RT_s}\right) \tag{A.13}$$

$$S_{dev,tar} = m_{dry\_wood} A_{devo,tar} \exp\left(\frac{E_{dev,tar}}{RT_s}\right) \tag{A.14}$$

$$S_{dev,char} = m_{dry\_wood} A_{devo,char} \exp\left(\frac{E_{dev,char}}{RT_s}\right) \tag{A.15}$$

$$S_{dev,dry\_wood} = -S_{dev,gas} - S_{dev,tar} - S_{dev,char} \tag{A.16}$$

$$S_{charc,char} = -\left(1-\alpha\right) C_{O2,\infty} \Omega k_{eff} SA_{char} M_c \tag{A.17}$$

It should be noted that the char conversion front is assumed to be very thin. Thus, in the current implementation, the char conversion is only calculated in one cell, where the char front is currently located. SA_{char} can be estimated using the geometrical surface area of the char front, since the apparent kinetic formulation is applied.

The total energy source term (S_{energy}, J/s) has contributions from drying ($S_{energy,dry}$, J/s), devolatilization ($S_{energy,dev}$, J/s), and char conversion ($S_{energy,charc}$, J/s), which are calculated as follows:

$$S_{energy} = S_{energy,dry} + S_{energy,dry} + S_{energy,charc} \tag{A.18}$$

$$S_{energy,dry} = MC_{wb} S_{dry,wet\_wood} \left(c_{p,H2O}\left(T_{s,boundary} - T_s\right) + \Delta H_{dry}\right) \tag{A.19}$$

$$S_{energy,dev} = -\left(S_{dev,gas} + S_{dev,tar}\right) c_{p,vol}\left(T_{s,boundary} - T_s\right) + S_{dev,dry\_wood} \Delta H_{dev} \tag{A.20}$$

$$S_{energy,charc} = S_{charc,char} \Delta H_{charc} \tag{A.21}$$

where ΔH_{dry}, ΔH_{dev}, and ΔH_{charc} are latent heat of vaporization of water, heat of devolatilization, and heat of reaction due to char conversion, respectively (J/kg); $c_{p,H2O}$ and $c_{p,vol}$ are heat capacities of water vapor and volatiles, respectively (J/kg K). As explained in Section 2.2, the energy source term is linearized using Picard's method:

$$S_{energy} = S_u + S_p T_s \tag{A.22}$$

where the superscript $*$ represents values in the current time step.

$$S_u = S^*_{energy} - \left(\frac{\partial S_{energy}}{\partial T_s}\right)^* T^*_s \tag{A.23}$$

$$S_p = \left(\frac{\partial S_{energy}}{\partial T_s}\right)^* \tag{A.24}$$

The update of the particle temperature is performed in three steps. First, the particle surface temperature is determined by solving the heat balance over the particle surface as:

$$h\Gamma_{sur}\left(T_g - T_{sur}\right) + \varepsilon\sigma\Gamma_{sur}\left(\theta^4 - T^4_{sur}\right) = \kappa_{Np-1} SA_{sur} \frac{dT_s}{dr}\bigg|_{xc_{Np}, xc_{Np-1}} \tag{A.25}$$

where h is the convective heat transfer coefficient (J/m^2 K s), which is estimated using Ranz-Marshall Correlation, σ is the Stefan Boltzmann constant (kg/s^3 K^4), θ is the radiation temperature (K) which is estimated by the reactor wall temperature in the particle simulation, and SA_{sur} is particle surface area (m^2).

Thereafter, the linearized temperature equations are established as:

$$\begin{bmatrix} a_{P,Np-1} & a_{E,Np-1} & & & & & & \\ a_{W,Np-2} & a_{P,Np-2} & a_{E,Np-2} & & & & & \\ & \dots & \dots & \dots & & & & \\ & & a_{W,i} & a_{P,i} & a_{E,i} & & & \\ & & & \dots & \dots & \dots & & \\ & & & & a_{W,1} & a_{P,1} & a_{E,1} & \\ & & & & & a_{W,0} & a_{P,0} & \end{bmatrix} \begin{bmatrix} T_{s,Np-1} \\ T_{s,Np-2} \\ \dots \\ T_{s,i} \\ \dots \\ T_{s,1} \\ T_{s,0} \end{bmatrix} = \begin{bmatrix} b_{Np-1} \\ b_{Np-2} \\ \dots \\ b_i \\ \dots \\ b_1 \\ b_0 \end{bmatrix} \tag{A.26}$$

where a and b are matrix coefficients which can be calculated as:

$$a_{P,i} = \begin{cases} -\frac{m_{p,i}c_{p,i}}{dt} - \frac{SA_{b,i-1}\frac{\kappa_i+\kappa_{i-1}}{2}}{xc_i - xc_{i-1}} & i = Np-1, \text{outermostcell} \\ -\frac{SA_{sur}\kappa_i}{rb - xc_i} + S_{p,i} & \\ -\frac{m_{p,i}c_{p,i}}{dt} - \frac{SA_{b,i-1}\frac{\kappa_i+\kappa_{i-1}}{2}}{xc_i - xc_{i-1}} & 0 < i < Np-1 \\ -\frac{SA_{b,i}\frac{\kappa_{i+1}+\kappa_i}{2}}{xc_{i+1} - xc_i} + S_{p,i} & \\ -\frac{m_{p,i}c_{p,i}}{dt} - \frac{SA_{b,i}\frac{\kappa_{i+1}+\kappa_i}{2}}{xc_{i+1} - xc_i} + S_{p,i} & i = 0, \text{innermostcell} \end{cases} \tag{A.27}$$

$$a_{E,i} = \begin{cases} \frac{SA_{b,i-1}\frac{\kappa_i+\kappa_{i-1}}{2}}{xc_i - xc_{i-1}} & 0 < i \leq Np-1 \\ 0 & i = 0, \text{innermostcell} \end{cases} \tag{A.28}$$

$$a_{W,i} = \begin{cases} 0 & i = Np-1, \text{outermostcell} \\ \frac{SA_{b,i}\frac{\kappa_{i+1}+\kappa_i}{2}}{xc_{i+1} - xc_i} & 0 \leq i < Np-1 \end{cases} \tag{A.29}$$

$$b_i = \begin{cases} -\frac{m_{p,i}c_{p,i}}{dt}T^0_{s,i} - \frac{SA_{sur}\kappa_i}{(rb - xc_i)}T_{sur} - S_{u,i} & i = Np-1, \text{outermostcell} \\ -\frac{m_{p,i}c_{p,i}}{dt}T^0_{s,i} - S_{u,i} & 0 \leq i < Np-1 \end{cases} \tag{A.30}$$

where the SA_b is the surface area of the cell outer boundary (west boundary, m^2). The matrix system is solved by LU factorization using a matrix solver named Meschach. More details regarding the matrix solver can be found from `http://homepage.divms.uiowa.edu/~dstewart/meschach/`. After the temperatures have been solved for, the mass of each species in each cell is then updated by:

$$m_{wet\_wood} = m^0_{wet\_wood} + S_{dry,wet\_wood}dt \tag{A.31}$$

$$m_{dry\_wood} = m^0_{dry\_wood} + S_{dev,dry\_wood}dt - S_{dry,wet\_wood}dt\,(1 - MC_{wb}) \tag{A.32}$$

$$m_{char} = m^0_{char} + S_{charc,char}dt + S_{dev,char}dt \tag{A.33}$$

$$m_{ash} = m^0_{ash} - w_{char,ash}S_{charc,char}dt \tag{A.34}$$

Depending on whether the current time reaches the given end time or not, the code either advances to the next time step or terminates.

Appendix B

In this section, the effect of thermal conductivity of char (κ_{char}) is illustrated in Figure B.1 and Figure B.2. It should be noted that the calculated center temperature shown in Figure B.1(b) is represented by the temperature of the innermost layer, which is higher than the actual center temperature. A previous study has shown that IBMs can better estimate the temperature

of the center with an additional constant core layer [6], the application of which is outside the scope of the current work.

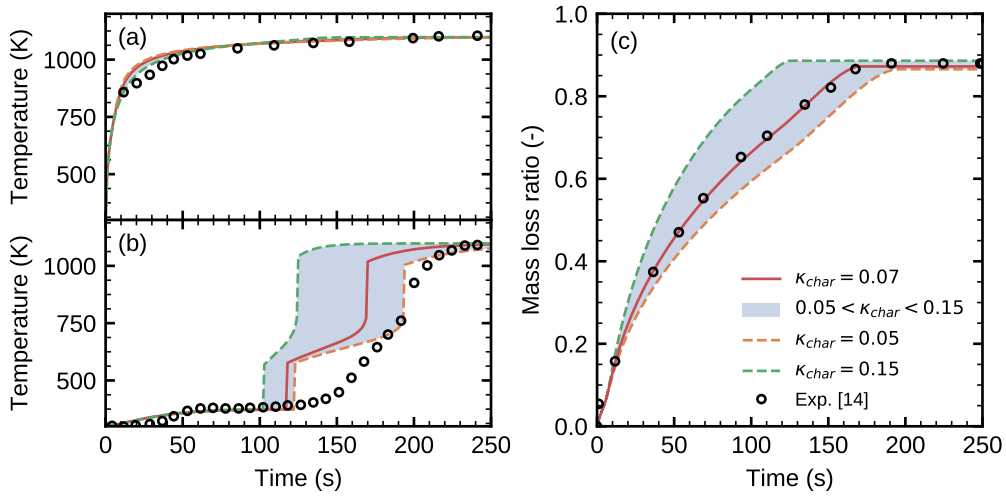

Figure B.1: Calculated (with IBM 1) and measured surface temperature profile (a), center temperature profile (b), and particle mass loss ratio (c) during pyrolysis of a beech particle ($d = 9.5$ mm, $T_w = T_g = 1098$ K, $MC_{wb} = 20\%$, $\phi_{N2} = 100\%$).

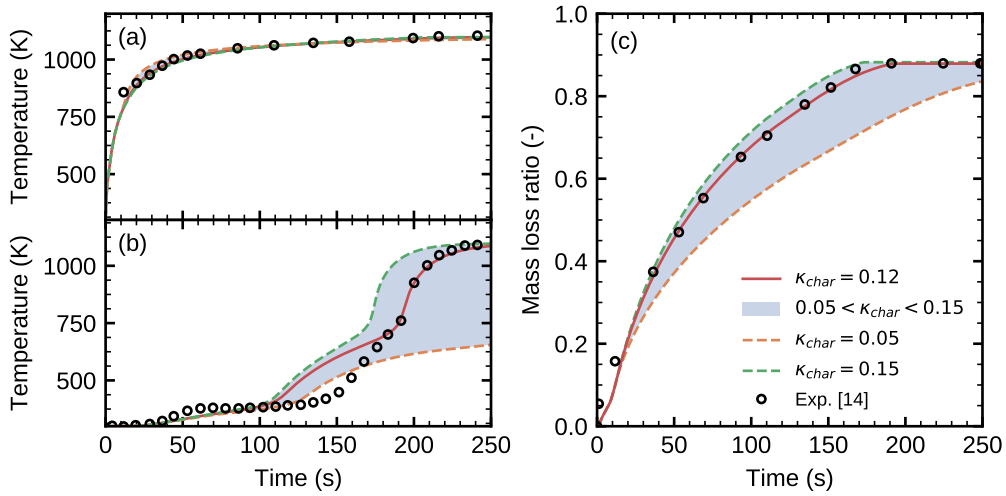

Figure B.2: Calculated (with the proposed MBM) and measured surface temperature profile (a), center temperature profile (b), and particle mass loss ratio (c) during pyrolysis of a beech particle ($d = 9.5$ mm, $T_w = T_g = 1098$ K, $MC_{wb} = 20\%$, $\phi_{N2} = 100\%$).

References

References

[1] H.-S. Helmisaari, L. Kaarakka, B. A. Olsson, Increased utilization of different tree parts for energy purposes in the Nordic countries, Scandinavian Journal of Forest Research 29 (2014) 312–322.

[2] J. M. Johansen, P. A. Jensen, P. Glarborg, M. Mancini, R. Weber, R. E. Mitchell, Extension of apparent devolatilization kinetics from thermally thin to thermally thick particles in zero dimensions for woody biomass, Energy 95 (2016) 279–290.

[3] I. Haberle, Ø. Skreiberg, J. Łazar, N. E. L. Haugen, Numerical models for thermochemical degradation of thermally thick woody biomass, and

their application in domestic wood heating appliances and grate furnaces, Progress in Energy and Combustion Science 63 (2017) 204–252.

[4] R. Johansson, H. Thunman, B. Leckner, Influence of intraparticle gradients in modeling of fixed bed combustion, Combustion and Flame 149 (1-2) (2007) 49–62.

[5] H. Thunman, B. Leckner, F. Niklasson, F. Johnsson, Combustion of wood particles — A particle model for Eulerian calculations, Combustion and Flame 129 (1-2) (2002) 30–46.

[6] H. Ström, H. Thunman, CFD simulations of biofuel bed conversion: A submodel for the drying and devolatilization of thermally thick wood particles, Combustion and Flame 160 (2) (2013) 417–431.

[7] R. Mehrabian, S. Zahirovic, R. Scharler, I. Obernberger, S. Kleditzsch, S. Wirtz, V. Scherer, H. Lu, L. L. Baxter, A CFD model for thermal conversion of thermally thick biomass particles, Fuel Processing Technology 95 (2012) 96–108.

[8] J. Saastamoinen, J.-r. Richard, Simultaneous drying and pyrolysis of solid fuel particles, Combustion and Flame 106 (3) (1996) 288–300.

[9] A. Galgano, C. Di Blasi, Modeling the propagation of drying and decomposition fronts in wood, Combustion and Flame 139 (1-2) (2004) 16–27.

[10] K. M. Bryden, M. J. Hagge, Modeling the combined impact of moisture and char shrinkage on the pyrolysis of a biomass particle, Fuel 82 (13) (2003) 1633–1644.

[11] S. S. Alves, J. L. Figueiredo, A model for pyrolysis of wet wood, Chemical Engineering Science 44 (12) (1989) 2861–2869.

[12] M. C. Melaaen, Numerical analysis of heat and mass transfer in drying and pyrolysis of porous media, Numerical Heat Transfer, Part A: Applications 29 (4) (1996) 331–355.

[13] C. Di Blasi, Heat, momentum and mass transport through a shrinking biomass particle exposed to thermal radiation, Chemical Engineering Science 51 (7) (1996) 1121–1132.

[14] J. C. Wurzenberger, S. Wallner, H. Raupenstrauch, J. G. Khinast, Thermal conversion of biomass: Comprehensive reactor and particle modeling, AIChE Journal 48 (10) (2002) 2398–2411.

[15] H. Lu, W. Robert, G. Peirce, B. Ripa, L. L. Baxter, Comprehensive study of Biomass particle combustion, Energy & Fuels 22 (4) (2008) 2826–2839.

[16] H. Fatehi, F. M. Schmidt, X.-S. Bai, Gas phase combustion in the vicinity of a biomass particle during devolatilization – Model development and experimental verification, Combustion and Flame 196 (2018) 351–363.

[17] H. Fatehi, X.-S. Bai, A Comprehensive Mathematical Model for Biomass Combustion, Combustion Science and Technology 186 (2014) 574–593.

[18] M. A. Gómez, J. Porteiro, D. Patiño, J. L. Míguez, Fast-solving thermally thick model of biomass particles embedded in a CFD code for the

simulation of fixed-bed burners, Energy Conversion and Management 105 (2015) 30–44.

[19] S. Hermansson, H. Thunman, CFD modelling of bed shrinkage and channelling in fixed-bed combustion, Combustion and Flame 158 (5) (2011) 988–999.

[20] R. Issa, B. Ahmadi-Befrui, K. Beshay, A. Gosman, Solution of the implicitly discretised reacting flow equations by operator-splitting, Journal of Computational Physics 93 (2) (1991) 388–410.

[21] A. Imren, D. Haworth, On the merits of extrapolation-based stiff ODE solvers for combustion CFD, Combustion and Flame 174 (2016) 1–15.

[22] H. K. Versteeg, W. Malalasekera, An Introduction to Computational Fluid Dynamics: The Finite Volume Method, Pearson Education Limited, England, 2007.

[23] D. E. Stewar, Z. Leyk, Meschach: Matrix computations in C, Proceedings of the Centre for Mathematics and Its Applications 32.

[24] E. S. Oran, J. P. Boris, Numerical simulation of reactive flow, 2nd Edition, Cambridge University Press, 2005.

[25] A. Alamia, H. Ström, H. Thunman, Design of an integrated dryer and conveyor belt for woody biofuels, Biomass and Bioenergy 77 (2015) 92–109.

[26] E. Ranzi, A. Cuoci, T. Faravelli, A. Frassoldati, G. Migliavacca,

S. Pierucci, S. Sommariva, Chemical Kinetics of Biomass Pyrolysis, Energy & Fuels 22 (6) (2008) 4292–4300.

[27] P. E. A. Debiagi, C. Pecchi, G. Gentile, A. Frassoldati, A. Cuoci, T. Faravelli, E. Ranzi, Extractives Extend the Applicability of Multistep Kinetic Scheme of Biomass Pyrolysis, Energy and Fuels 29 (10) (2015) 6544–6555.

[28] S. Niksa, Predicting the rapid devolatilization of diverse forms of biomass with bio-flashchain, Proceedings of the Combustion Institute 28 (2) (2000) 2727–2733.

[29] A. D. Lewis, T. H. Fletcher, Prediction of Sawdust Pyrolysis Yields from a Flat-Flame Burner Using the CPD Model, Energy & Fuels 27 (2) (2013) 942–953.

[30] Y. Chen, S. Charpenay, A. Jensen, M. A. Wójtowicz, M. A. Serio, Modeling of biomass pyrolysis kinetics, Symposium (International) on Combustion 27 (1) (1998) 1327–1334.

[31] C. Diblasi, Modeling chemical and physical processes of wood and biomass pyrolysis, Progress in Energy and Combustion Science 34 (1) (2008) 47–90.

[32] B. Wagenaar, W. Prins, W. Swaaij, Flash pyrolysis kinetics of pine wood, Fuel processing technology 36 (1993) 291–298.

[33] B. Peters, Thermal Conversion of Solid Fuels, WIT Press, Southampton, UK, 2003.

[34] D. Evans, H. Emmons, Combustion of wood charcoal, Fire Safety Journal 1 (1) (1977) 57–66.

[35] H. Yan, O. Fujita, Study of the transient combustion of highly densified biomass briquette (Bio-coke) in an air flow, Fuel 188 (2017) 595–602.

[36] M. El Houssami, A. Lamorlette, D. Morvan, R. M. Hadden, A. Simeoni, Framework for submodel improvement in wildfire modeling, Combustion and Flame 190 (2018) 12–24.

[37] H. Fatehi, X. S. Bai, Structural evolution of biomass char and its effect on the gasification rate, Applied Energy 185 (2017) 998–1006.

[38] A. H. Mahmoudi, F. Hoffmann, M. Markovic, B. Peters, G. Brem, Numerical modeling of self-heating and self-ignition in a packed-bed of biomass using XDEM, Combustion and Flame 163 (2016) 358–369.

[39] N. T. Duffy, J. A. Eaton, Investigation of factors affecting channelling in fixed-bed solid fuel combustion using CFD, Combustion and Flame 160 (10) (2013) 2204–2220.

[40] A. N. Hayhurst, M. S. Parmar, Measurement of the mass transfer coefficient and sherwood number for carbon spheres burning in a bubbling fluidized bed, Combustion and Flame 130 (2002) 361–375.

[41] J. S. Dennis, A. N. Hayhurst, S. A. Scott, The combustion of large particles of char in bubbling fluidized beds: The dependence of Sherwood number and the rate of burning on particle diameter, Combustion and Flame 147 (2006) 185–194.

[42] Forest Products Laboratory, Wood handbook—Wood as an engineering material, Tech. rep., U.S. Department of Agriculture, Forest Service, Forest Products Laboratory, Madison, WI (1999).

[43] R. Kumar, A. Kolar, B. Leckner, Shrinkage characteristics of Casuarina wood during devolatilization in a fluidized bed combustor, Biomass and Bioenergy 30 (2) (2006) 153–165.

[44] H. Thunman, B. Leckner, Thermal conductivity of wood—models for different stages of combustion, Biomass and Bioenergy 23 (1) (2002) 47–54.

[45] H. Thunman, F. Niklasson, F. Johnsson, B. Leckner, Composition of volatile gases and thermochemical properties of wood for modeling of fixed or fluidized beds, Energy and Fuels 15 (6) (2001) 1488–1497.

[46] K. Ragland, D. Aerts, A. Baker, Properties of wood for combustion analysis, Bioresource Technology 37 (2) (1991) 161–168.

[47] M. P. Remacha, S. Jiménez, J. Ballester, Devolatilization of millimeter-sized biomass particles at high temperatures and heating rates. Part 1: Experimental methods and results, Fuel 234 (2018) 757–769.

[48] W. H. McAdams, Heat Transmission, 3rd Edition, Mcgraw - Hill Book Company, 1954.

[49] F. He, F. Behrendt, A new method for simulating the combustion of a large biomass particle—A combination of a volume reaction model and front reaction approximation, Combustion and Flame 158 (12) (2011) 2500–2511.

[50] C. Yin, L. Rosendahl, S. K. Kær, Grate-firing of biomass for heat and power production, Progress in Energy and Combustion Science 34 (6) (2008) 725–754.

[51] H. Ström, F. Niklasson, A. Hjörnhede, S. Hermansson, Experimental and numerical investigations of ash behaviour in fixed-bed combustion of woody biomass pellets, Industrial Combustion Journal 11.

[52] P. Jop, Y. Forterre, O. Pouliquen, A constitutive law for dense granular flows, Nature 441 (7094) (2006) 727–730.